Fluid assisted strain localization in quartz at the brittle/ductile transition

Samuele Papeschi[1,2] and Giovanni Musumeci[2,3]

1. Dipartimento di Scienze della Terra, Firenze University, via la Pira 4, 50121 Firenze, Italy

2. Dipartimento di Scienze della Terra, Pisa University, via Santa Maria 53, 56126 Pisa, Italy

3. Istituto Nazionale di Geofisica e Vulcanologia, via della Faggiola 32, 56126 Pisa, Italy

Corresponding author: Samuele Papeschi (s.papeschi@gmail.com)

Key Points:

- Strain partitioning between recrystallized grains and 'stiff' quartz porphyroclasts;
- Fracturing and fluid ingress assist propagation of shear bands;
- Authigenesis of new quartz and phyllosilicate grains from circulating fluids promotes strain localization on shear bands;

Abstract

A mylonitic quartzite with conjugate and synthetic shear bands was investigated by Electron BackScatter Diffraction (EBSD) and optical microscopy to obtain insights on recrystallization mechanisms and strain localization in quartz at plastic to semibrittle conditions close to the brittle-ductile transition. The mylonitic quartzite deformed during Late Miocene thrusting coeval with contact metamorphism in the high-strain domains of the Calamita Schists (Elba Island, Italy). Mylonitic deformation occurred from amphibolite to lower greenschist facies conditions during cooling of the aureole. Dynamic recrystallization, dominated by the activity of dislocation creep by prism <a> slip, produced recrystallized quartz layers mantling relic large quartz porphyroclasts. Under decreasing temperature and fluid-rich conditions, quartz porphyroclasts acted as relatively rigid bodies and fractured along synthetic and conjugate C' shear bands. Shear bands developed along kinematically favored orientations, just locally assisted by weak crystallographic planes in quartz. Fracturing along shear bands was assisted by cataclasis and fluid infiltration enhancing fracture propagation and healing by recrystallization and authigenesis of new quartz and phyllosilicate grains. The process likely operated in a cyclical fashion enhancing propagation of and strain localization in shear bands, with the development of bands of 'weak' phyllosilicates. Furthermore, we observed the development of a CPO related to dissolution and precipitation of new grains parallel to shear bands. This study highlights the importance of the interplay between brittle and crystal-plastic processes and fluid ingress in the semibrittle regime to understand deformation partitioning and strain localization.

Plain Language Summary

Quartz is one of the main constitutive minerals of the Earth's rocks and largely controls how rock deform. We used the optical microscope to investigate quartz and a special technique called EBSD, that is based on the interaction between a beam of electrons and a crystalline material, to generate maps of how quartz crystals are oriented in space, in order to investigate quartz deformation. We studied rocks that were heated up to 650 °C six million years ago by a chamber of molten magma and at the same time were squeezed by tectonic forces in the Calamita peninsula (Elba Island, Italy). During cooling from such high temperatures, deformation in quartz was first accommodated by plastic mechanisms, like metal warped by a blacksmith, producing large quartz crystals wrapped by newly formed smaller quartz crystals. Subsequently, at lower temperatures (~ 300 – 400 °C), deformation in cool large quartz crystals started to produce cracks and fractures. As fractures opened, high temperature water-rich fluids flooded the fractures, encrusting them with tiny quartz and platy mica crystals. This process likely operated multiple times, progressively leading to the development of bands of 'weak' platy micas in 'hard' quartz crystals.

1. Introduction

Deformation in shear zones is accommodated by brittle, frictional mechanisms in the upper crust and by plastic mechanisms at higher temperature in the lower crust. The transition between purely brittle to purely crystal-plastic deformation in natural shear zones occurs over a wide range of temperature conditions at which deformation is controlled by a combination of brittle and plastic mechanisms (semibrittle deformation; Evans & Kohlstedt, 1995; Kohlstedt et al., 1995). A classic example is represented by sheared quartz-feldspar aggregates at mid-crustal conditions, where quartz typically recrystallizes and feldspar forms fractured porphyroclasts (Vernon & Flood, 1988; Tullis et al., 1990, 2000). Quartz at mid-crustal conditions (300 – 450 °C) is typically thought to deform by dislocation creep (Hirth & Tullis, 1994; Gleason & Tullis, 1995; Stipp et al., 2002; Behr & Platt, 2011, 2014). However, many studies focused on quartz monomineralic aggregates highlighted the complex role played by grain scale strain partitioning causing semibrittle deformation in quartz (van Daalen et al., 1999; Vernooij et al., 2006a, b; Muto et al., 2011). Intra-grain bands of deformation in quartz, typically constituted by trails of small grains hosted by larger grains, have been classically described as the result of the interplay between brittle and crystal-plastic processes. Their development has been alternatively explained as the result of failure along the rhomb planes of quartz (van Daalen et al., 1999; Vernooij et al., 2006a,b), coalescence of microfractures developed along specific crystallographic planes (Trepmann & Stöckhert, 2003; Trepmann et al., 2007) or localized coaxial deformation in 'stiff' domains (Menegon et al., 2008). Several contrasting mechanisms have been proposed to explain the growth of new grains in such bands: (1) subgrain rotation followed by rigid-body rotation of grains (Bestmann & Prior, 2003; Ceccato et al., 2017; Trepmann et al., 2017), (2) cataclasis and healing by recrystallization (den Brok, 1992; van Daalen et al., 1999; Vernooij et al., 2006a,b), (3) dissolution-precipitation creep, with solution of material which is precipitated as new grains (Hippertt & Egydio-Silva, 1996; Takeshita & Hara, 1998; Takeshita & El-Fakharani, 2013; Kjøll et al., 2015) and (4) recrystallization along mechanically formed Dauphiné twins (Stipp & Kunze, 2008; Menegon et al., 2011). These structures have also been shown to form during the earthquake cycle immediately below the brittle-ductile transition (Trepmann & Stöckhert, 2003; Trepmann et al., 2007, 2017).

In this study, we present an EBSD based investigation of the development and evolution of intra-grain shear bands in quartz in the semibrittle regime, investigated in a natural study case represented by a cooling contact aureole (Papeschi et al., 2017, 2018). The research presented here highlights how grain-scale contrasts drive strain partitioning from the early stages of dynamic recrystallization to the brittle regime and how the interplay between brittle and crystal-plastic processes with intergranular fluids may assist softening and strain localization in shear bands that may efficiently act as precursory structures for discrete faults.

2. Geological Outline

Elba Island, located in the northern Thyrrhenian Sea, exposes a complete cross section through the hinterland sector of the northern Apennines belt. The nappe pile is characterized by east-verging structures stacked over W-dipping top-to-the-E thrust sheets during the Early Miocene (Keller & Coward, 1996; Massa et al., 2017). The nappe stack comprises an Upper Complex, characterized by ophiolite-bearing oceanic and continental units with anchizone to lower greenschist facies metamorphism, and a Lower Complex, consisting of the upper greenschist to amphibolite facies Ortano and Calamita Units (Fig. 1a). Blueschist facies metamorphism related to Early Miocene underthrusting and nappe stacking is locally preserved in the Ortano Unit (Bianco et al., 2015). However, the dominant metamorphic imprint is the Late Miocene LP/HT metamorphism related to the emplacement of granitic bodies, coeval with the late phase of east-verging thrusting (Duranti et al., 1992; Musumeci & Vaselli, 2012; Musumeci et al., 2015; Viola et al., 2018).

The Calamita Schists, part of the Calamita Unit (Fig. 1a), are an amphibolite facies metapsammitic complex that crop out in SE Elba Island (Barberi et al., 1967). These rocks experienced Miocene deformation and LP/HT metamorphism triggered by the intrusion of the buried Porto Azzurro pluton (Papeschi et al., 2017) with peak temperatures around 625 °C (Caggianelli et al., 2018) or exceeding 650 °C (Musumeci & Vaselli, 2012) at pressure lower than 0.2 GPa (Duranti et al., 1992). Deformation, related to the activity of thrust sheets coeval with pluton emplacement, affected the Calamita Schists at upper crustal conditions during post-magmatic cooling.

Geochronological data constraint ductile shearing between 6.8 – 6.3 Ma (Musumeci et al., 2015) and the subsequent brittle deformation between 6.1 and 4.9 Ma (Viola et al., 2018), indicating that the equilibration to upper crustal temperature occurred in less than 1 Ma. Deformation was heterogeneously distributed in top to the east ductile shear zones that recorded the transition from an upper amphibolite facies foliation to a greenschist facies mylonitic foliation, overprinted at the brittle/ductile transition by brittle fault zones and shear fractures. These latter cross cut the mylonitic foliation exploiting precursory ductile shear bands (Papeschi et al., 2017, 2018).

The Praticciolo Cape (Fig. 1b; see details in Papeschi et al., 2018) offers a natural cross sections through mylonitic quartzites and micaschists belonging to the Calamita Schists, tectonically overlain by metacarbonate rocks over the flat segment of a large-scale east-verging thrust (Fig. 1b). Here, the Calamita Schists are characterized by a well-developed W-dipping foliation (mean dip-direction/dip: N261°/33°), a stretching lineation defined by quartz and phyllosilicate aggregates (trend/plunge: N255°/32°) and synthetic and conjugate sets of C' shear bands (synthetic set: N250°/03°; antithetic set: N227°/72°) (Fig. 1c). Shear fractures and brittle fault zones (N156°/01°), parallel to C' shear bands (Fig. 1d), cross cut the foliation and represents the last deformation structures developed. For the present study, a mylonitic quartzite sample (sample IESP3SP78 highlighted in Fig. 1b) have been selected for fabric analysis.

3. Analytical Method

Standard oriented thin sections (i.e. cut orthogonal to the foliation and parallel to the stretching lineation) were investigated using the optical microscope and the Scanning Electron Microscope (SEM), and for Electron Back Scatter Diffraction (EBSD) analysis of the quartz microfabric (see Prior et al., 1999).

Thin sections were polished using an alkaloid colloidal suspension (SYTON) with a Buehler Vibromet 2 for at least 3 hours and then carbon coated to about 3.5 nm thickness. EBSD maps were acquired at the Electron Microscope Centre of Plymouth University with a (1) JEOL 6610 LV SEM equipped with a NordLys Nano EBSD detector and a (2) JEOL 7001 FEG SEM equipped with a NordLys Max EBSD detector, using a 20-25 mm working distance, 70° of sample tilt with respect to the horizontal and accelerating voltage set at 20 keV. The sample symmetry used was monoclinic and quartz was the only phase indexed, using trigonal crystal system (Laue group 3/m). EBSD patterns were automatically detected and indexed with the software AZTec (Oxford Instruments). The step size used and the size of the EBSD map frame are provided for each map in the corresponding figure (Fig. 4a, 6a and 8a). Noise reduction, following Bestmann & Prior (2003), was performed using the HKL CHANNEL 5 software (Oxford Instruments). The critical misorientation for the definition of high angle boundaries (shown in black in orientation maps) was set at 10°, allowing grain boundary completion down to 0°, and at 2-10° for low-angle boundaries (in white). Dauphiné twin boundaries (in red; Frondel et al., 1962) were recognized as grain boundaries with 60° ± 2° of misorientation and <c> as misorientation axis and disregarded from the grain detection procedure. Grain size was obtained using the grain detection routine of Channel 5 (Tango software) that recalculates grain diameters (μm) from equivalent area circles (μm^2) (as in Berger & Herwegh, 2004). As a rule, grains measuring less than 3 times the step size (i.e. containing less than 4-9 pixels) were nullified.

Pole figures and misorientation axis orientations in sample coordinates (MOSC) are equal angle, lower hemisphere projections oriented with respect to the finite strain ellipsoid reference frame (X = lineation; Z = pole to the foliation). Inverse pole figures and misorientation axis orientations in crystal coordinates (MOCC) are equal area, upper hemisphere projections. Contoured pole figures (one-point-per-grain) were performed using 10° half width and 10° cluster size with density shown as multiples of a uniform distribution (MUD). The misorientation axis distribution in crystal coordinates (or MOCC) is a powerful tool to guess the active slip system(s) in a crystal lattice. Following Lloyd and Freeman (1994) and Neumann (2000), if we assume the ideal activity of edge dislocations associated with a slip system the misorientation axis (i.e. axis of rotation with the smallest rotation angle among equivalent rotation relating two given orientations of an object; Moriawiec, 2004) is (1) contained in the slip plane and (2) oriented perpendicular to the Burgers vector. A scheme showing the misorientation axes and related slip systems for quartz (after Neumann, 2000) is reported in Fig. 2.

4. Microstructural and EBSD Analysis

4.1 Sample Description

The investigated mylonitic quartzite sample (IESP3SP78; Fig. 1b) shows a well-developed foliation (oriented N220°/24°) defined by the subparallel disposition of quartz and phyllosilicate layers (Fig. 3a). The kinematics is top-to-the-E, defined by asymmetric objects at the meso- and microscale and by S-C' structures. The foliation is cut and offset by two sets of C' shear bands: a dominant top-to-the-E set (C'1), subhorizontal and synthetic with respect to the sample kinematics, and a less-developed top-to-the-W antithetic set, which is steeply dipping at the mesoscale (N227°/72°).

At the microscale, phyllosilicate layers are very fine-grained (<< 5 µm) and almost exclusively constituted by sericite and chlorite mixed with tiny (< 5 µm) quartz grains and accessory ilmenite and magnetite that surround fractured and sericitized andalusite and cordierite porphyroclasts (50-

200 µm). Large chlorite stacks (up to 200 µm), biotite relics and white mica grains (grain size: 10 – 100 µm) are locally preserved in coarse-grained quartz lenses.

Quartz shows a strongly heterogeneous microstructure, consisting of a variable percentage of relic quartz porphyroclasts, either organized in lenses (e.g. Fig. 3b) or present as isolated grains lacking a clear preferred orientation (e.g. Fig. 3c), surrounded by aggregates (e.g. Fig. 3c) and well-defined subparallel layers of recrystallized quartz grains (e.g. Fig. 3a). Because of the marked microstructural differences observed within the quartz layers, we have studied in detail several domains, each characterized by internally homogeneous microstructures. Three different domains have been identified, described individually and mapped by EBSD: Subparallel quartz layers (Domain 1; Fig. 3a), (2) quartz porphyroclasts with conjugate shear bands (Domain 2; Fig. 3b) and (3) quartz layers with synthetic shear bands (Domain 3; Fig. 3c).

4.2 Subparallel Quartz Layers

Subparallel quartz layers (Domain 1), ranging in thickness between 50 and 500 µm, are continuous and stretched parallel to the mylonitic foliation (Fig. 3a). Thin sericite bands (<< 5 µm grain size) and ellipsoidal phyllosilicate aggregates, the latter representing pseudomorphs over cordierite, occur interlayered with quartz (Fig. 3a). C' shear bands are uncommon and, when present, are localized in the phyllosilicate rich interlayers.

The quartz layer microstructure is dominated by small (10 – 100 µm) recrystallized grains with serrated grain boundaries enveloping sparse quartz porphyroclasts (up to 500 µm) with lobate boundaries and amoeboid shape variably stretched parallel to the foliation (Fig. 3a). Undulose to patchy extinction patterns are common in quartz porphyroclasts. Small white mica inclusions display evidence for pinning of quartz grain boundaries. Large areas of recrystallized grains appear extinct at the same polarizer orientation, indicating the presence of a CPO (see gypsum plate insert in Fig. 3a).

The EBSD analysis, carried out in an area representative of Domain 1 (Map 1 in Fig. 3a), image larger grains (100-300 μm grain size), interpreted as relic grains and showing amoeboid shape and relatively high aspect ratio (2-4), , defining a shape preferred orientation parallel to the foliation (Fig. 4a). Such grains are surrounded by smaller new grains (10-50 μm) with equidimensional shape and serrated grain boundaries (Fig. 4a). Discontinuous low-angle boundaries with lobate shape are contained in old grains and, to a lesser extent, in some of the new grains. Irregular Dauphiné twin boundaries are present in all grains.

The bulk c-axis distribution defines a Y-max with limited tails on the XY-plane, associated with <a> axes on the periphery, distributed along 6 regular maxima every 60 ° (Fig. 4b). The correlated distribution in the misorientation angle distribution (MAD) shows two strong maxima, one at low angle misorientations (2-10°; Fig. 9a) and the other for 55-60° (Fig. 9a). In crystal coordinates the misorientation axes for low misorientation angles (2 up to 30°) are clustered in correspondence of the c- axis and are partially spread over the acute rhombs (Fig. 4c). In sample coordinates, the maximum for low misorientation angles is localized defines a strong Y-max (Fig. 4d).

4.3 Conjugate Shear Bands

This domain (Domain 2) is represented by quartz lenses (grain size: 100-1000 μm; thickness: 100-200 μm up to some mm) constituted by large quartz porphyroclasts, surrounded by recrystallized quartz grains belonging to Domain 1 (Fig. 3b). Such lenses represent boudins of competent material (i.e. coarse-grained quartz) laterally bound by swells where the foliation is necked (Fig. 3b). Porphyroclast quartz grains feature extensive patchy to undulose extinction and host conjugate and roughly orthogonal C’ shear bands associated with irregular patterns of fractures (Fig. 3b). Conjugate shear bands are strictly localized in coarse-grained quartz porphyroclast and do not affect the neighboring fine-grained quartz layers and phyllosilicate domains, as shown in Fig. 3b. As shown in Fig. 5a, conjugate shear bands are defined by very fine-grained (<10-20 µm) trails of quartz. The host porphyroclast grains are fractured and feature fragments that have slightly different orientation (Fig. 5a). The contact between host grains and shear bands is marked by slightly misoriented areas and by small quartz trails with different orientation with respect to the host and often displaying a c-axis preferred orientation (Fig. 5a). At the SEM, the shear bands are characterized by fluid inclusion planes enclosing grains and cracks (Fig. 5b). Pitted grain boundaries, indicative of fluid-present conditions during deformation (e.g. Mancktelow et al., 1998) are widespread (Fig. 5b). Small chlorite and white mica inclusions are locally present.

A representative EBSD area was selected at the intersection of two conjugate C’ shear bands hosted by quartz porphyroclasts (Map 2 in Fig. 3b). The misorientation angle distribution shows high values of relative frequency for the correlated distribution, corresponding to 2-15° and 55-60° of misorientation respectively (Fig. 9b). The EBSD map images large (>500 µm) grains (i.e. host grains) that contains two nearly orthogonal shear bands (dextral and sinistral as shown in Fig. 6a) defined by grains smaller than 50 µm (i.e. shear band grains) and characterized by variable along-strike thickness from 150 to 10 µm (Fig. 6a). Minor shear bands decorated by few tiny grains and oriented parallel to the larger ones are also present, like the small dextral band marked by a yellow arrow in Fig. 6a.

Host grains display wavy grain boundaries, locally associated with tiny grains and bulges (5-20 µm), and irregular Dauphiné twin boundaries that are cross cut by conchoidal fractures (Fig. 6a). In the pole figures, they display ‘single crystal’ orientations, with c-axes randomly clustered and

<a> axes and rhombs drawing small (20-40°) rotations, highlighting the internal distortion of the crystal lattice (Fig. 6b). Shear band grains range in size between 3 and 30 µm, forming heterogeneous aggregates that envelope larger grains with variable shape and size up to 100 µm. In pole figures, shear band grains are broadly characterized by host control, as they mimic the host grains orientation, and display a c-axis maximum in the upper-right quadrangle of the pole figure (Fig. 6c). As shown by misorientation profiles, large areas of shear band grains are slightly misoriented with respect to the host grains (less than 20-30°; Fig. 6d, e) and just some grains are characterized by high misorientation with respect to the host (Fig. 6e).

In crystal coordinates, host grains display a moderate clustering on the c-axis associated with minor scattering towards the rhomb, corresponding to a weak maxima developed in the lower-left quadrangle of the pole figure in sample coordinates (Fig. 6f). Shear band grains show clustering of the misorientation axis in sample coordinates close to <c> with a wider spreading towards the rhombs and the prism (Fig. 6g). In sample coordinates a weak maximum is present, close to Y in the upper-right quadrangle of the pole figure (Fig. 6g).

4.3.1 Relationships between shear bands and host grains

The attitude of the shear bands in Map 2 was compared with the orientation of the major lattice planes within selected host grains adjacent to shear bands (subsets numbered from 1 to 4 in Fig. 7a). The crystallographic orientation of the selected host grains was also compared with the crystallographic orientation of the grains associated with the dextral and sinistral shear bands (subsets highlighted in Fig. 7d). The dextral shear band separates the adjacent grains 1, 2 and 3, whereas the sinistral is localized between grains 3 and 4. Two grains with identical crystallographic orientation are present on the opposite sides of the sinistral shear band and interpreted to be originally part of the same grain (grain 4; Fig. 7a).

Host grains display c-axes oriented halfway between the periphery and the center of the pole figure (Fig. 7b). The trace of the shear bands does not evidently match most of the crystallographic planes of the selected host grains. A slight parallelism exists only between the trace of the sinistral shear band and the positive and negative rhomb planes of grain 3 and the basal plane of grain 4 (Fig. 7b). Other major crystallographic planes are oblique to shear bands. In crystal coordinates, the misorientation axis clusters in correspondence of the c-axis and the acute rhombs, with minor spreading close to {m} and (c), as in grain 1 and 4 (Fig. 7c). In sample coordinates, host grains display clustering away from Y with faint girdles (grain 1) and secondary maxima (grains 3 and 4; Fig. 7c).

The comparison of the c-axes of the sinistral and dextral shear band subsets (Fig. 7d) with that of their respective host grains shows that the c-axes of shear band grains cluster in the same orientation of those of their hosts (Fig. 7e). The distribution of the c-axes of shear band grains with respect to the host suggests a clockwise rotation consistent with the, local, dextral (Fig. 7e, above) and sinistral (Fig. 7e, below) sense of shear. Considering the sinistral shear band, a third cluster is located in the upper right quadrant of the pole figure, parallel to the sinistral shear band (Fig. 7e). This latter does is not related to any orientation observed in the neighboring host grains and is related to grains characterized by relative misorientation up to 70-90° with respect to the hosts i.e. as the grains intercepted by misorientation profile B (Fig. 6e).

4.4 Synthetic Shear Bands

Large areas of the sample are characterized by a single set of synthetic top-to-the-E C' shear bands (Domain 3), oriented ~30-35° with respect to the foliation that, differently from conjugate shear bands, does not appear restricted to coarse-grained quartz lenses but invariably affects quartz and phyllosilicate-rich layers (Fig. 3c). With respect to the subparallel quartz layers (Domain 1), the quartz layers where C' shear bands are more developed appear richer in large quartz porphyroclasts (grain size: 100 – 500 µm) with lensoidal shape and lobate grain boundaries that are surrounded by mantles of equigranular, recrystallized grains (5 – 50 µm) with serrated boundaries (Fig. 3c). Quartz porphyroclasts feature undulose extinction and serrated contacts with the recrystallized grains surrounding them and are often wrapped by strain caps rich in phyllosilicates or opaque mineral grains (Fig. 5c). Sometimes irregular intra-granular cracks are well developed in quartz porphyroclasts, dissecting angular sub-areas (Fig. 5c). Lens-shaped quartz aggregates are commonly dragged synthetically with the shear bands, defining an S-C' fabric (Fig. 3c). Synthetic shear bands are often developed within or at the contact with quartz porphyroclasts with spacing lower than the millimeter and offsets that may reach several hundreds of micrometers (Fig. 5d). Sometimes they are partially reactivated as small-scale shear fractures that are continuous for several millimeters through multiple mica and quartz layers characterized by millimetric offsets (Fig. 5d) and bridged by en-echelon subsidiary sets of fractures (Fig. 5d, see insert). The shear band architecture is characterized by a 50 – 100 µm thick core zone containing very fine-grained quartz grains (i.e. shear band grains), locally with a shape preferred orientation parallel to the band and a preferred orientation of the c-axis, associated with bands of tiny, platy white mica and chlorite grains oriented parallel to the shear band (Fig. 5e). As shown by the SEM image the core of the shear band displays cracks and fractures associated with fluid inclusion planes and pitted quartz grain boundary surfaces (Fig. 5f). Chlorite and white mica are locally associated with oxides (i.e. limonite; Fig. 5f) and found as single grains included in quartz (Fig. 5f). These features are indicative of fluid-rock interaction during deformation (e.g. Mancktelow et al., 1998).

The area to map by EBSD (Map 3 in Fig. 3c) has been positioned within two paired, synthetic, dextral shear bands cross cutting quartz and characterized by a total offset of ~500 µm. Since quartz is the only phase indexed, phyllosilicate-rich cores appear black (Fig. 8a). The large porphyroclast grains hosting the shear band (grain size > 100 µm; host grains in Fig. 8; appearing grey in Fig. 8d) are surrounded by small grains displaying grain size in the range 3 – 65 µm. The MAD shows high correlated frequencies for low angles of misorientation (<10°) and for 55-60° of misorientation (Fig. 9c).

Host grains display lobate to serrated boundaries with small bulges and are characterized by wriggly Dauphiné twin boundaries and relatively straight low-angle boundaries that separate subgrains of about 10 – 50 µm grain size (Fig. 8a). The c-axis of the host grains subset displays several 'single grain' orientations scattered on the pole figure and slightly clustered close to Y (Fig. 8b). Host grains are in first order mantled by new grains with equigranular shape, serrated boundaries, grain size ranging between 20 and 60 µm and aspect ratio between 1 and 1.5-1.6 (Fig. 8d).

The smaller grains of the dataset (< 5 – 20 µm; shear band grains in Fig. 8) occur localized on shear bands, largely associated with bands of phyllosilicates and characterized by an equigranular shape (Fig. 8d). In the pole figure two trends are recognizable in shear band grains: (1) a contouring generally inherited from the crystal orientation of the host grains (Fig. 8c; compare with Fig. 8d) and (2) a strong maximum developed in the upper-left quadrangle of the pole figure parallel to the shear band, in an orientation where no corresponding maximum associated with the host grains subset exists (Fig. 8c).

In crystal coordinates host grains display a strong clustering for 2-15° of misorientation angles around <c> which corresponds in sample coordinates to a misorientation axis maximum clustered on Y (Fig. 8e). Shear band grains are characterized in crystal coordinates by a weaker maximum with respect to the host grains clustered on <c> and a wider scattering towards the rhombs and the acute rhombs for 2-15° of misorientation angles (Fig. 8f). In sample coordinates they display clustering loosely centered on Y (Fig. 8f).

5. Discussion

5.1 Grain-scale strain partitioning in the different domains

Our data set documents an example of strain partitioning at the thin section scale in a quartz-dominated sample that was sheared during retrograde metamorphism from upper amphibolite to lower greenschist facies conditions. Close to peak metamorphic conditions deformation was likely accommodated by grain boundary migration recrystallization, as indicated by relic amoeboid grains and dissection microstructures (see in detail Papeschi et al., 2017). During cooling, dynamic recrystallization by subgrain rotation and bulging led to the development of a heterogeneous microfabric generally characterized by large quartz porphyroclasts and lenses embedded in a relatively fine-grained recrystallized quartz-rich matrix (Fig. 3). The high frequencies shown by the correlated MAD curve for low-angle misorientations is consistent with fabric development under conditions dominated by dislocation creep (Fig. 9a, b, c). The 55-60° peak, observed in all investigated maps, is related to Dauphiné twinning (Fig. 9). The c-axis clustering with limited spreading towards the rhombs of the misorientation axis in crystal coordinates observed for both host grains and recrystallized grains in the investigated EBSD areas (Fig. 4c, 6f, g , 8e, f) is consistent with the dominant activity of the prism <a> slip system, associated with secondary rhomb <a> slip (see Fig. 2 for reference). Though the dominant activity of prism <a> slip is witnessed in all the investigated maps, very different microstructures evolved in the different domains investigated. In Domain 1, deformation produced straight and parallel recrystallized quartz layers (Fig. 3a), whereas in Domains 2-3 large quartz porphyroclasts survived (Fig. 3b, c), leading to the development of sets of shear bands. Two major mechanisms are believed to have controlled the development of such diverse microstructures: (1) grain scale strain partitioning leading to a completely different microfabric evolution within the different domains and (2) fluid ingress and fluid-rock interaction, as documented by the abundant pitted grain boundaries, trails of fluid inclusions and secondary phases trapped in quartz (Fig. 5; e.g. Drury & Urai, 1990; Mancktelow et al., 1998; Mancktelow & Pennacchioni, 2004).

Domain 1 is characterized by large areas that are extinct at the same time (Fig. 3a) corresponding to portions where relic and recrystallized grains contributing to define a typical Y-max texture (Schmidt & Casey, 1986; Fig. 4b). In this domain large relic grains were compliant during deformation developing a high aspect ratio and a preferred orientation parallel to the foliation, as it is expected for grains with c-axis parallel to Y under conditions of dominant prism <a> slip (e.g. Muto et al., 2011; Ceccato et al., 2017). The favorable orientation of the recrystallizing material assisted recrystallization at low stresses favoring the development of a strong CPO (Fig. 3a). On the other hand, in Domain 2 and 3, the presence of large grains with c-axis orthogonal or oblique to Y (Fig. 6b, 8b) disadvantaged dislocation creep by dominant prism <a> slip. Secondary slip systems, such as rhomb <a> (e.g. grain 2-3 in Fig. 7c) or basal <a> slip (e.g. grain 1 in Fig. 7c) might have locally activated as their misorientation axis was lying closer to the vorticity axis Y for those grains (e.g. Michels et al., 2015). Nevertheless, the activation of slip systems differing from prism <a> slip was energetically unfavored and grains with c-axis oriented far from Y were less stress compliant during dynamic recrystallization compared to the Y-grains of Domain 1. Therefore, deformation likely localized in recrystallized portions surrounding the 'hardened' porphyroclast grains that acted as the main strain-supporting framework leaving behind coarse-grained pods and lenses (Fig. 3b, c). Large quartz porphyroclasts behaved as relatively hard domains, fracturing and concentrating strain in conjugate and synthetic shear bands. The development of conjugate sets of shear bands in quartz has been described by several authors as a result of fracturing along planes of weakness such as the rhombs (van Daalen et al., 1999; Vernooij et al., 2006a, b; Kjøll et al., 2015). The analysis of the shear band attitude performed by Papeschi et al. (2018) indicate a nearly constant orientation through the sample which is not compatible with the local orientation of quartz rhomb planes. Moreover, the investigate conjugate shear bands are just locally parallel to planes of weakness in quartz such as the rhombs (Fig. 7a, b), indicating little to no host control during their development. Conjugate shear bands in coarse-grained quartz domains may develop after deformation partitioning, as a result of coaxial deformation localizing in 'hard' domains surrounded by a non-coaxially deforming matrix, as suggested by Menegon et al. (2008) in the Arolla Unit; on the other hand, they might be developed during general shear close to the direction of maximum shear stress or to the eigenvectors of the flow (e.g. Bobyarchick, 1986; Simpson & de Paor, 1993; Kurz & Northrup, 2008; Gillam et al., 2014), as suggested for the Calamita Schists by Papeschi et al. (2018). In this sense, the conjugate sets may be preferentially developed in large and relatively isotropic quartz lenses, as the presence of a strong mechanical anisotropy (i.e. the mylonitic foliation) outside inhibits the development of the steeper set, as shown by Cobbold et al. (1971), Cobbold (1976) and Platt and Vissers (1980).

5.2 Role of fluids and dynamic recrystallization in shear band development

Formation of shear bands at greenschist to amphibolite facies conditions has classically been associated with a combination of brittle and crystal-plastic processes (Berthé et al., 1979; Gapais & White, 1982; Passchier, 1984; Gapais, 1989; van Daalen et al., 1999; Vernooij et al., 2006a,b). In the present study case, evidence for intra-granular microcracking is invariably found as fractures and fluid inclusion planes (Fig. 3b, 5b, c, f) in quartz porphyroclasts that occur in strict association with conjugate and synthetic shear bands. Cataclasis, accompanied by rigid-body rotation of host quartz grains fragments may explain the weak misorientation of shear band grains with respect to the host, highlighted by pole figures (Fig. 6c, 8c) and by misorientation profiles (Fig. 6d, e), and the inhomogeneous grain size of shear band grains (Fig. 6a, 8d). Rigid-body rotation is also consistent with the local clockwise and anticlockwise rotation of shear band grains with respect to the host in sinistral and dextral shear band respectively (Fig. 7e). Host grains are characterized by a distorted lattice with clustering on <c> in crystal coordinates, indicative of dominant prism <a> slip, centered on Y in sample coordinates (Fig. 6f, 8e). These patterns are largely inherited as intracrystalline features by shear band grains, although there is evidence of an increased activity of rhomb <a> slip (Fig. 6g, 8f; see Fig. 2 for reference). After microcracking and rigid-body rotation, fluid ingress might have favored dynamic recrystallization and healing of microcracks, sealing deformation in the shear band. Evidence for fluid-accompanied fracturing is supported by the presence of pitted grain boundaries and trails of fluid inclusions (Fig. 5b), as well as many secondary phases trapped in quartz (Fig. 5e, f); see e.g. Drury & Urai, 1990; Mancktelow et al., 1998; Mancktelow & Pennacchioni, 2004). Shear bands might have deformed cyclically accommodated by multiple cycles of cracking and sealing assisted by fluid ingress in a similar fashion as the example described by Kjøll et al. (2015) and rapidly followed by dynamic recrystallization as described by van Daalen et al. (1999) in the Glarus Nappe and experimentally by Vernooij et al. (2006a, b).

Nevertheless, this process cannot fully explain the development of CPOs oriented parallel to shear bands associated with the smaller grains (Fig. 6c, 8c) that would require the activity of prism <c> slip and should be discouraged under conditions favoring prism and rhomb <a> slip. Furthermore, this CPO is related to grains strongly misoriented with respect to the host (up to 70° in misorientation profiles; Fig. 6d, e) and is developed in an orientation which cannot be inherited from the host grains population (Fig. 7e). Bons and den Brok (2000) showed numerically how CPOs in rocks may develop as a result of dissolution-precipitation creep or pressure solution with the growth of new grains controlled by specific crystallographic directions. We suggest that the CPO in our investigated sample was controlled by the preferred growth of quartz grains with c-axes parallel to shear bands, which followed the opening of small dilatant sites during deformation. The process might have also been associated with pressure solution of quartz, as in strain caps surrounding larger porphyroclasts (e.g. Fig. 5c), readily redeposited in fractures sealing shear bands. This interpretation extends previous data gathered by Takeshita and Hara (1998) and Takeshita and El-Fakharani (2013), who observed the development of random textures by dissolution-precipitation, showing that precipitation of new grains from fluids may also cause the development of a CPO.

The precipitation of very fine-grained quartz and, in particular, 'weak' phyllosilicates may have assisted progressive strain softening of shear bands, enhancing grain size reduction (e.g. White et al., 1980; Behrmann & Mainprice, 1987; Fliervoet et al., 1997) and reaction softening (e.g. White et al., 1980; Stünitz & Tullis, 2001; Bukovskà et al., 2016). In particular, inclusions of phyllosilicates organized in bands (Fig. 5e) are widespread along synthetic C' shear bands that occur indeed not restricted to large quartz porphyroclasts (Fig. 3c) and show larger eastward displacements with respect to the conjugate set. The feedback between deformation, fluid-rock interaction and chemical processes controlled the progressive organization of phyllosilicate grains in bands on the synthetic set, promoting slip.

To summarize, the observed quartz microstructure of C' shear bands can be explained as resulting from the combination of two mechanisms: (1) microfracturing and rigid-body rotation of fragments separated from the parent grain, (2) dynamic recrystallization and healing associated with (3) authigenesis of quartz and phyllosilicate grains from circulating intergranular fluids with the development of a CPO in quartz parallel to the shear bands.

5.3 From dynamic recrystallization to strain localization in the semibrittle regime

The data set presented here documents the progressive development of deformation structures in a quartz-rich system at the transition from purely plastic to purely brittle deformation under fluid-rich conditions (see also Papeschi et al., 2017, 2018). The structural evolution, controlled in first order by the decreasing temperature during deformation, is conceptually summarized in Fig. 10. At relatively high metamorphic grade conditions (amphibolite facies; Musumeci & Vaselli, 2012; Caggianelli et al., 2018) quartz recrystallized producing stretched mylonitic ribbons (Fig. 10). Deformation concentrated in first order in recrystallized portions, leaving behind large quartz porphyroclasts, where dislocation creep was recorded as intracrystalline deformation (Fig. 10). As temperature progressively decreased, large quartz relics underwent hardening with respect to the surrounding 'soft' quartz + phyllosilicate matrix, fracturing along conjugate shear bands (Fig. 10). Opening of intra-granular cracks allowed fluid infiltration and the consequent authigenesis of new quartz and phyllosilicate grains. This occurred under greenschist facies conditions, as indicated by the white mica + chlorite + opaque assemblage that is invariably found on shear bands (Fig. 5), although early precursory cracking might have opened even earlier. Fluid ingress may also have aided fracture propagation by mechanisms such as stress corrosion cracking or microplasticity (Atkinson, 1984; Kerrich, 1986; Stünitz & Fitz Gerald, 1993). Transient surges in pore fluid pressure or strain rate may have also promoted fracturing and fluid ingress in a cyclical fashion, followed by recrystallization and precipitation of new grains, as shown e.g. by Kjøll et al. (2015). Slip on antithetic shear bands was hindered by their steeper orientation with respect to the mylonitic foliation, promoting strain localization on the synthetic set (Fig. 10). As slip accumulated on synthetic C' shear bands, more fluids were called in, activating a positive feedback mechanisms that enhanced lubrication by continuous authigenesis of 'soft' phyllosilicates organized in subparallel bands (Fig. 3c, d). A similar process was documented in quartz-feldspathic rocks of the South Armorican Shear Zone by Bukovskà et al. (2016), who documented shear band propagation by fluid infiltration promoting reaction softening at lower greenschist facies conditions. Propagation of shear bands outside of the coarse and 'stiff' quart porphyroclasts might have likely promoted by temperature decrease, as basal <a> slip is energetically favored at low temperature conditions but no evidence for it was found in the analyzed domains, suggesting that the presence of strong Y-max textures possibly hindered dislocation creep by basal <a> slip (geometric hardening; Poirier, 1980; Toy et al., 2008), forcing early strain localization in phyllosilicate-rich layers and shear bands. Finally, following the embrittlement of the system below the brittle-ductile transition for quartz (i.e. 310 ± 30 °C; Stöckhert et al., 1999; 280 ± 30 °C; Stipp et al., 2002), the presence of bands of phyllosilicates in shear bands oriented obliquely to the mylonitic foliation formed a 'weak' network acting as ductile precursors (Fig. 1c) for faults and shear fractures (Fig. 1d), as documented by Papeschi et al. (2018) and, in the studied sample, by shear fractures locally connecting and reactivating shear bands (Fig. 5d). At this stage, slip on the mylonitic foliation is halted and top-to-the-E deformation starts to be accommodated by non-Andersonian faults, discordant over the foliation.

6. Conclusions

The microstructures presented in this paper contribute to the understanding of the switch from purely crystal-plastic to semibrittle deformation in quartz, showing how shear bands may develop and act as precursors for brittle structures. The data shown here supports previous studies on the subject and adds further constraints by showing the following:

1. At high grade metamorphic conditions, the dominant activity of a slip system, in this case prism <a> slip, promotes deformation in grains that are efficiently oriented for slip, leaving behind porphyroclasts that remain relatively undeformed, wrapped by the soft mylonitic matrix.
2. In the semibrittle regime, deformation partitioning promotes fracturing and cataclasis along conjugate and synthetic shear bands in 'hard' quartz porphyroclasts, while deformation in the mylonitic foliation is still controlled by dislocation creep. The direction exploited for fracturing is not necessarily coincident with crystallographic planes of weakness but is pre-determined by the vorticity of the flow.
3. Under fluid rich conditions, fluid ingress assists propagation, healing of fractures by recrystallization and authigenesis of new quartz and phyllosilicate grains in microfractures. The process may operate cyclically, assisting slip on shear bands and enhancing strain softening with the formation of bands of 'soft' tiny quartz and phyllosilicates. The opening

of dilatant sites during slip promoted fluid infiltration and authigenesis of quartz grains with a CPO parallel to shear bands.

4. Progressive strain localization on shear bands was likely favored by the geometric hardening of mylonitic ribbons and the progressive interconnection of shear band segments. In the brittle regime, faulting reactivates shear bands, concentrating slip on structures discordant to the foliation.

Acknowledgements

Luca Menegon is warmly thanked for assistance and guidance with the EBSD analysis and for hosting at the Plymouth University (U.K.). The staff at Plymouth Electron Microscopy Centre is thanked for the technical support. Giulia degli Alessandrini, Simone Papa and Lucy Campbell are thanked for discussion and assistance with the EBSD software. Financial support from the University of Pisa (PRA 2016 Resp. Sergio Rocchi) and travel support from the PEGASO PhD Programme of the Tuscany Region is acknowledged. EBSD map source files are available at http://dx.doi.org/10.17632/4vrhnw44zr.1#file-1e9730b1-dd12-49b1-aa2c-99ea85963788.

References

Atkinson, B.K., 1984. Subcritical crack growth in geological materials. *Journal of Geophysical Research: Solid Earth, 89*(B6), 4077-4114.

Barberi, F., Innocenti, F., & Ricci, C.A., 1967. Il complesso scistoso di Capo Calamita (Isola d'Elba). *Atti della Società Toscana di Scienze Naturali, Memorie, Serie A, 74*, 579-617.

Behr, W. M., & Platt, J. P., 2011. A naturally constrained stress profile through the middle crust in an extensional terrane. *Earth and Planetary Science Letters*, *303*(3-4), 181-192.

Behr, W.M., & Platt, J.P., 2014. Brittle faults are weak, yet the ductile middle crust is strong: Implications for lithospheric mechanics. *Geophysical Research Letters*, *41*(22), 8067-8075.

Behrmann, J.H., & Mainprice, D., 1987. Deformation mechanisms in a high-temperature quartz-feldspar mylonite: evidence for superplastic flow in the lower continental crust. *Tectonophysics*, *140*(2-4), 297-305.

Berger, A., & Herwegh, M., 2004. Grain coarsening in contact metamorphic carbonates: effects of second-phase particles, fluid flow and thermal perturbations. *Journal of Metamorphic Geology*, *22*(5), 459-474.

Berthé, D., Choukroune, P., & Jégouzo, P., 1979. Orthogneiss, mylonite and non coaxial deformation of granites: the example of the South Armorican Shear Zone. *Journal of Structural Geology*, *1*(1), 31-42.

Bestmann, M., & Prior, D.J., 2003. Intragranular dynamic recrystallization in naturally deformed calcite marble: diffusion accommodated grain boundary sliding as a result of subgrain rotation recrystallization. *Journal of Structural Geology*, *25*(10), 1597-1613.

Bianco, C., Brogi, A., Caggianelli, A., Giorgetti, G., Liotta, D., & Meccheri, M., 2015. HP-LT metamorphism in Elba Island: implications for the geodynamic evolution of the inner Northern Apennines (Italy). *Journal of Geodynamics*, *91*, 13-25.

Bobyarchick, A. R., 1986. The eigenvalues of steady flow in Mohr space. *Tectonophysics*, *122*(1-2), 35-51.

Bons, P.D., & den Brok, B., 2000. Crystallographic preferred orientation development by dissolution–precipitation creep. *Journal of Structural Geology, 22*(11-12), 1713-1722.

Bousquet, R., Goffé, B., Vidal, O., Oberhänsli, R., & Patriat, M., 2002. The tectono-metamorphic history of the Valaisan domain from the Western to the Central Alps: New constraints on the evolution of the Alps. *Geological Society of America Bulletin, 114*(2), 207-225.

den Brok, S. W. J., 1992. *An experimental investigation into the effect of water on the flow of quartzite*. Utrecht University, Holland.

Bukovská, Z., Jeřábek, P., & Morales, L.F., 2016. Major softening at brittle-ductile transition due to interplay between chemical and deformation processes: An insight from evolution of shear bands in the South Armorican Shear Zone. *Journal of Geophysical Research: Solid Earth, 121*(2), 1158-1182.

Caggianelli, A., Zucchi, M., Bianco, C., Brogi, A., & Liotta, D., 2018. Estimating PT metamorphic conditions on the roof of a hidden granitic pluton: an example from the Mt. Calamita promontory (Elba Island, Italy). *Italian Journal of Geosciences, 137*(2), 238-253.

Cathelineau, M. & Nieva, D., 1985. A chlorite solid solution geothermometer the Los Azufres (Mexico) geothermal system. *Contributions to Mineralogy and Petrology*, *91*(3), pp.235-244.

Ceccato, A., Pennacchioni, G., Menegon, L., & Bestmann, M., 2017. Crystallographic control and texture inheritance during mylonitization of coarse grained quartz veins. *Lithos, 290*, 210-227.

Cobbold, P.R., Cosgrove, J.W., & Summers, J.M., 1971. Development of internal structures in deformed anisotropic rocks. *Tectonophysics*, *12*(1), 23-53.

Cobbold, P., 1976. Mechanical effects of anisotropy during large finite deformations. *Bulletin de la Société gèologique de France, 7*(6), 1497-1510.

van Daalen, M., Heilbronner, R., & Kunze, K., 1999. Orientation analysis of localized shear deformation in quartz fibres at the brittle–ductile transition. *Tectonophysics, 303*(1-4), 83-107.

Deer, W.A., Howie, R.A. & Zussman, J, 1992. *An introduction to the rock forming minerals, second Ed.* Longman Group Ltd, New York.

Drury, M.R., & Urai, J.L., 1990. Deformation-related recrystallization processes. *Tectonophysics, 172*(3-4), 235-253.

Duranti, S., Palmeri, R., Pertusati, P.C., & Ricci, C.A., 1992. Geological evolution and metamorphic petrology of the basal sequences of eastern Elba (complex II). *Acta Vulcanologica*, *2*, 213-229.

Evans, B., & Kohlstedt, D.L., 1995. Rheology of rocks. In: Ahrens, T.J. (Eds.), *Rock Physics and Phase Relations: A Handbook of Physical Constants*, AGU Ref. Shelf, 3, pp.148-165.

Fliervoet, T.F., White, S.H., & Drury, M.R., 1997. Evidence for dominant grain-boundary sliding deformation in greenschist-and amphibolite-grade polymineralic ultramylonites from the Redbank Deformed Zone, Central Australia. *Journal of Structural Geology, 19*(12), 1495-1520.

Frondel, C., 1962. *The system of mineralogy, seventh ed., vol III, silica minerals*. Wiley, New York.

Gapais, D., 1989. Shear structures within deformed granites: mechanical and thermal indicators. *Geology, 17*(12), 1144-1147.

Gapais, D., & White, S. H., 1982. Ductile shear bands in a naturally deformed quartzite. *Texture, Stress, and Microstructure*, *5*(1), 1-17.

Gillam, B. G., Little, T. A., Smith, E., & Toy, V. G., 2014. Reprint of Extensional shear band development on the outer margin of the Alpine mylonite zone, Tatare Stream, Southern Alps, New Zealand. *Journal of Structural Geology, 64*, 115-134.

Gleason, G.C., Tullis, J., 1995. A flow law for dislocation creep of quartz aggregates determined with the molten salt cell. *Tectonophysics, 247*(1-4), 1-23.

Hippertt, J., & Egydio-Silva, M., 1996. New polygonal grains formed by dissolution-redeposition in quartz mylonite. *Journal of Structural Geology, 18*(11), 1345-1352.

Hirth, G., & Tullis, J., 1994. The brittle-plastic transition in experimentally deformed quartz aggregates. *Journal of Geophysical Research: Solid Earth, 99*(B6), 11731-11747.

Keller, J.V.A., & Coward, M.P., 1996. The structure and evolution of the Northern Tyrrhenian Sea. *Geological Magazine, 133*(1), 1-16.

Kerrich, R., 1986. Fluid infiltration into fault zones: chemical, isotopic, and mechanical effects. *Pure and applied geophysics, 124*(1-2), 225-268.

Kjøll, H.J., Viola, G., Menegon, L., & Sørensen, B.E., 2015. Brittle-viscous deformation of vein quartz under fluid-rich lower greenschist facies conditions. *Solid Earth, 6*(2), 681-699.

Kohlstedt, D.L., Evans, B., & Mackwell, S.J., 1995. Strength of the lithosphere: Constraints imposed by laboratory experiments. *Journal of Geophysical Research: Solid Earth*, *100*(B9), 17587-17602.

Kurz, G. A., & Northrup, C. J., 2008. Structural analysis of mylonitic rocks in the Cougar Creek Complex, Oregon–Idaho using the porphyroclast hyperbolic distribution method, and potential use of SC′-type extensional shear bands as quantitative vorticity indicators. *Journal of Structural Geology*, *30*(8), 1005-1012.

Lister, G.S., & Snoke, A.W., 1984. SC mylonites. *Journal of Structural Geology, 6*(6), 617-638.

Lloyd, G.E., & Freeman, B., 1994. Dynamic recrystallization of quartz under greenschist conditions. *Journal of Structural Geology, 16*(6), 867-881.

Mancktelow, N.S., Grujic, D., & Johnson, E.L., 1998. An SEM study of porosity and grain boundary microstructure in quartz mylonites, Simplon Fault Zone, Central Alps. *Contributions to Mineralogy and Petrology*, *131*(1), 71-85.

Mancktelow, N.S., & Pennacchioni, G., 2004. The influence of grain boundary fluids on the microstructure of quartz-feldspar mylonites. *Journal of Structural Geology*, *26*(1), 47-69.

Massa, G., Musumeci, G., Mazzarini, F., & Pieruccioni, D., 2017. Coexistence of contractional and extensional tectonics during the northern Apennines orogeny: the late Miocene out-of-sequence thrust in the Elba Island nappe stack. *Geological Journal, 52*(3), 353-368.

Menegon, L., Pennacchioni, G., Heilbronner, R., & Pittarello, L., 2008. Evolution of quartz microstructure and c-axis crystallographic preferred orientation within ductilely deformed granitoids (Arolla unit, Western Alps). *Journal of Structural Geology*, *30*(11), 1332-1347.

Menegon, L., Piazolo, S., & Pennacchioni, G., 2011. The effect of Dauphiné twinning on plastic strain in quartz. *Contributions to Mineralogy and Petrology*, *161*(4), 635-652.

Michels, Z. D., Kruckenberg, S. C., Davis, J. R., & Tikoff, B., 2015. Determining vorticity axes from grain-scale dispersion of crystallographic orientations. *Geology*, *43*(9), 803-806.

Morawiec, A., 2004. *Misorientation Angle and Axis Distributions*. Springer, Berlin, Heidelberg.

Musumeci, G., & Vaselli, L., 2012. Neogene deformation and granite emplacement in the metamorphic units of northern Apennines (Italy): Insights from mylonitic marbles in the Porto Azzurro pluton contact aureole (Elba Island). *Geosphere*, *8*(2), 470-490.

Musumeci, G., Mazzarini, F., & Cruden, A.R., 2015. The Zuccale Fault, Elba Island, Italy: a new perspective from fault architecture. *Tectonics, 34*(6), 1195-1218.

Muto, J., Hirth, G., Heilbronner, R., & Tullis, J., 2011. Plastic anisotropy and fabric evolution in sheared and recrystallized quartz single crystals. *Journal of Geophysical Research: Solid Earth*, *116*(B2).

Neumann, B., 2000. Texture development of recrystallised quartz polycrystals unravelled by orientation and misorientation characteristics. *Journal of Structural Geology*, *22*(11-12), 1695-1711.

Papeschi, S., Musumeci, G., & Mazzarini, F., 2017. Heterogeneous brittle-ductile deformation at shallow crustal levels under high thermal conditions: The case of a synkinematic contact aureole in the inner northern Apennines, southeastern Elba Island, Italy. *Tectonophysics*, *717,* 547-564.

Papeschi, S., Musumeci, G., & Mazzarini, F., 2018. Evolution of shear zones through the brittle-ductile transition: The Calamita Schists (Elba Island, Italy). *Journal of Structural Geology,* 113, 100-114.

Passchier, C. W., 1984. The generation of ductile and brittle shear bands in a low-angle mylonite zone. *Journal of Structural Geology*, *6*(3), 273-281.

Platt, J. P., & Vissers, R. L. M., 1980. Extensional structures in anisotropic rocks. *Journal of Structural Geology*, *2*(4), 397-410.

Poirier, J. P., 1980. Shear localization and shear instability in materials in the ductile field. *Journal of Structural Geology*, *2*(1-2), 135-142.

Prior, D.J., Boyle, A.P., Brenker, F., Cheadle, M.C., Day, A., Lopez, G., et al., 1999. The application of electron backscatter diffraction and orientation contrast imaging in the SEM to textural problems in rocks. *American Mineralogist, 84*(11-12), 1741-1759.

Ralser, S., Hobbs, B.E., & Ord, A., 1991. Experimental deformation of a quartz mylonite. *Journal of Structural Geology*, *13*(7), 837-850.

Schmid, S.M., & Casey, M., 1986. Complete fabric analysis of some commonly observed quartz c-axis patterns. *Mineral and rock deformation: Laboratory studies*, *36*, 263-286.

Simpson, C., & de Paor, D. G., 1993. Strain and kinematic analysis in general shear zones. *Journal of Structural Geology*, *15*(1), 1-20.

Stipp, M., & Kunze, K., 2008. Dynamic recrystallization near the brittle-plastic transition in naturally and experimentally deformed quartz aggregates. *Tectonophysics, 448*(1-4), 77-97.

Stipp, M., Stünitz, H., Heilbronner, R., & Schmid, S.M., 2002. The eastern Tonale fault zone: a ‘natural laboratory’ for crystal plastic deformation of quartz over a temperature range from 250 to 700 C. *Journal of Structural Geology, 24*(12), 1861-1884.

Stöckhert, B., Brix, M.R., Kleinschrodt, R., Hurford, A.J., & Wirth, R., 1999. Thermochronometry and microstructures of quartz—a comparison with experimental flow laws and predictions on the temperature of the brittle–plastic transition. *Journal of Structural Geology, 21*(3), 351-369.

Stünitz, H., & Fitz Gerald, J., 1993. Deformation of granitoids at low metamorphic grade. II: Granular flow in albite-rich mylonites. *Tectonophysics*, *221*(3-4), 299-324.

Stünitz, H., & Tullis, J., 2001. Weakening and strain localization produced by syn-deformational reaction of plagioclase. *International Journal of Earth Sciences, 90*(1), 136-148.

Takeshita, T., & Hara, I., 1998. c-Axis fabrics and microstructures in a recrystallized quartz vein deformed under fluid-rich greenschist conditions. *Journal of Structural Geology, 20*(4), 417-431.

Takeshita, T., & El-Fakharani, A.H., 2013. Coupled micro-faulting and pressure solution creep overprinted on quartz schist deformed by intracrystalline plasticity during exhumation of the Sambagawa metamorphic rocks, southwest Japan. *Journal of Structural Geology, 46,* 142-157.

Toy, V.G., Prior, D.J., & Norris, R.J., 2008. Quartz fabrics in the Alpine Fault mylonites: Influence of pre-existing preferred orientations on fabric development during progressive uplift. *Journal of Structural Geology, 30*(5), 602-621.

Trepmann, C. A., & Stöckhert, B., 2003. Quartz microstructures developed during non-steady state plastic flow at rapidly decaying stress and strain rate. *Journal of Structural Geology, 25*(12), 2035-2051.

Trepmann, C.A., Stöckhert, B., Dorner, D., Moghadam, R.H., Küster, M., & Röller, K., 2007. Simulating coseismic deformation of quartz in the middle crust and fabric evolution during postseismic stress relaxation—an experimental study. *Tectonophysics*, *442*(1-4), 83-104.

Trepmann, C.A., Hsu, C., Hentschel, F., Döhler, K., Schneider, C., & Wichmann, V., 2017. Recrystallization of quartz after low-temperature plasticity–The record of stress relaxation below the seismogenic zone. *Journal of Structural Geology*, *95*, 77-92.

Tullis, J., Dell'Angelo, L., & Yund, R. A., 1990. Ductile shear zones from brittle precursors in feldspathic rocks: the role of dynamic recrystallization. In: Hobbs, B. E., Heard, H. C. (Eds.) Mineral and rock deformation: laboratory studies. *Geophysical Monograph Series*, *56*, 67-81.

Tullis, J., Stünitz, H., Teyssier, C., & Heilbronner, R. (2000). Deformation microstructures in quartzo-feldspathic rocks. In: Jessell, M.W., Urai, J. (Eds.) Stress, strain and structure; a volume in honor of W.D. Means. *Journal of the Virtual Explorer*, *2*.

Vernooij, M.G., Kunze, K., & den Brok, B., 2006a. 'Brittle' shear zones in experimentally deformed quartz single crystals. *Journal of Structural Geology*, *28*(7), 1292-1306.

Vernooij, M.G., den Brok, B., & Kunze, K., 2006b. Development of crystallographic preferred orientations by nucleation and growth of new grains in experimentally deformed quartz single crystals. *Tectonophysics*, *427*(1-4), 35-53.

Viola, G., Torgersen, E., Mazzarini, F., Musumeci, G., van der Lelij, R., Schönenberger, J., & Garofalo, P.S., 2018. New Constraints on the Evolution of the Inner Northern Apennines by K-Ar Dating of Late Miocene-Early Pliocene Compression on the Island of Elba, Italy. *Tectonics, 37*(9), 3229-3243.

Vernon, R. H., & Flood, R. H., 1988. Contrasting deformation of S-and I-type granitoids in the Lachlan fold belt, eastern Australia. *Tectonophysics*, *147*(1-2), 127-143.

White, S.H., Burrows, S.E., Carreras, J., Shaw, N.D., & Humphreys, F.J., 1980. On mylonites in ductile shear zones. *Journal of Structural Geology*, *2*(1-2), 175-187.

Figures

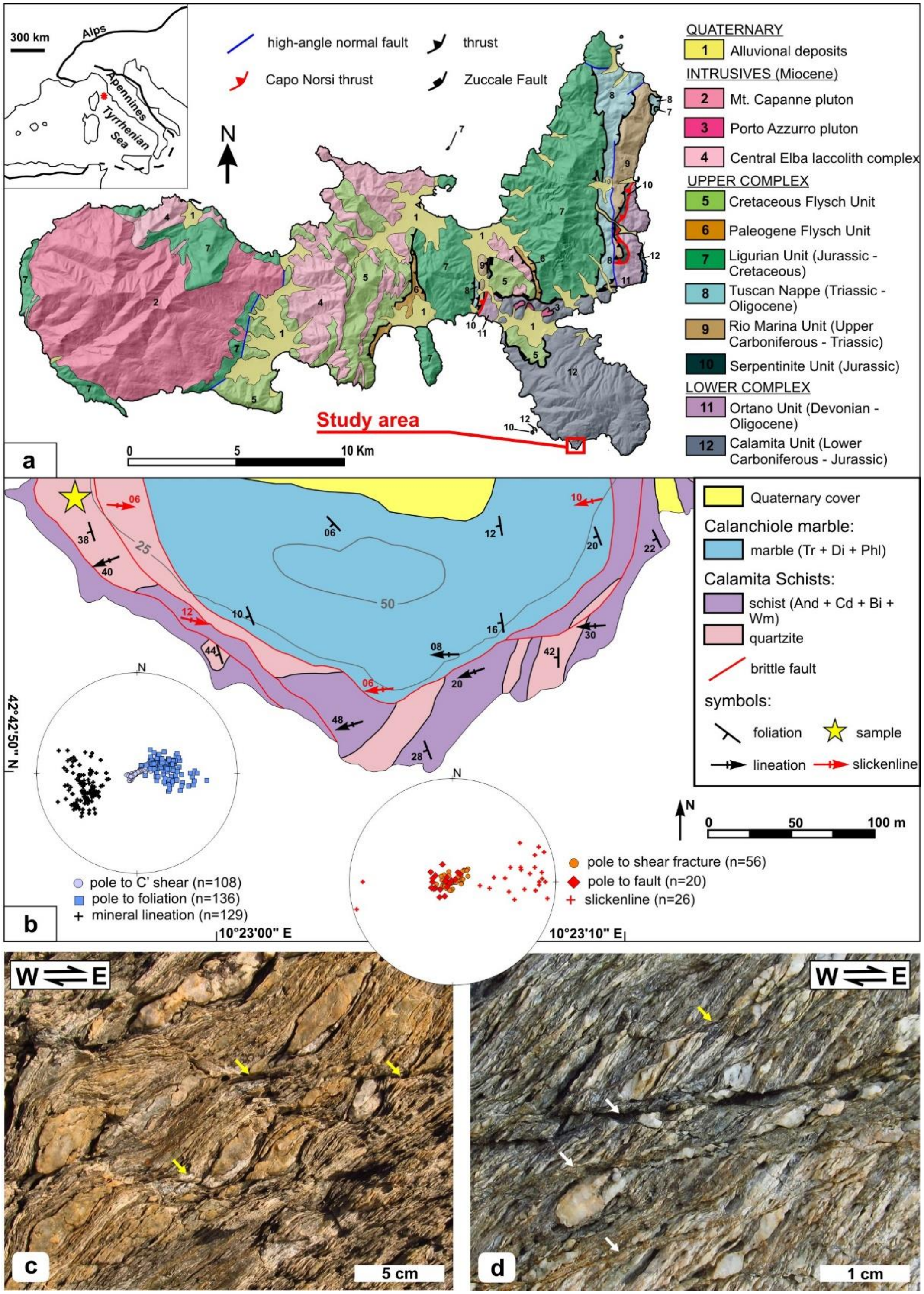

Figure 1 – (a) Simplified geological map of the Elba Island (modified after Massa et al., 2017) showing the location of the study area. **(b)** Sketch structural-geological map of the study area (Praticciolo Cape). Insert stereographic projections are in equal angle, lower hemisphere. The

yellow star marks the location of sample IESP3SP78. Mesoscale structures of the Calamita Schists at the Praticciolo: **(c)** well foliated top-to-the-E mylonitic micaschists with S-C' fabric and **(d)** top-to-the-E shear fractures cross cutting the mylonitic fabric and developed subparallel to C' shear bands. Yellow arrows: C' shear bands; white arrows: shear fractures.

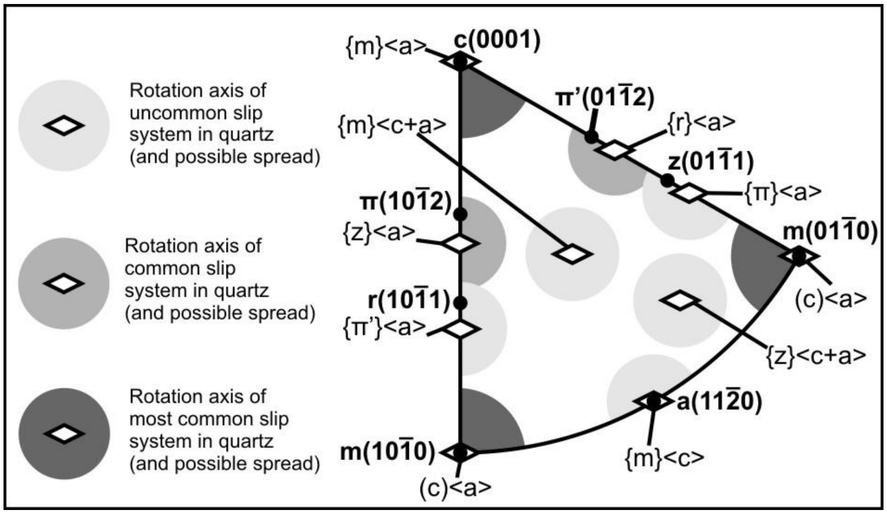

Figure 2 – Sketch illustrating the relationships between position of misorientation axis clustering in crystal coordinates and rotation axis of uncommon (light grey), common (grey) and most common (dark grey) slip systems in quartz. Modified after Neumann (2000).

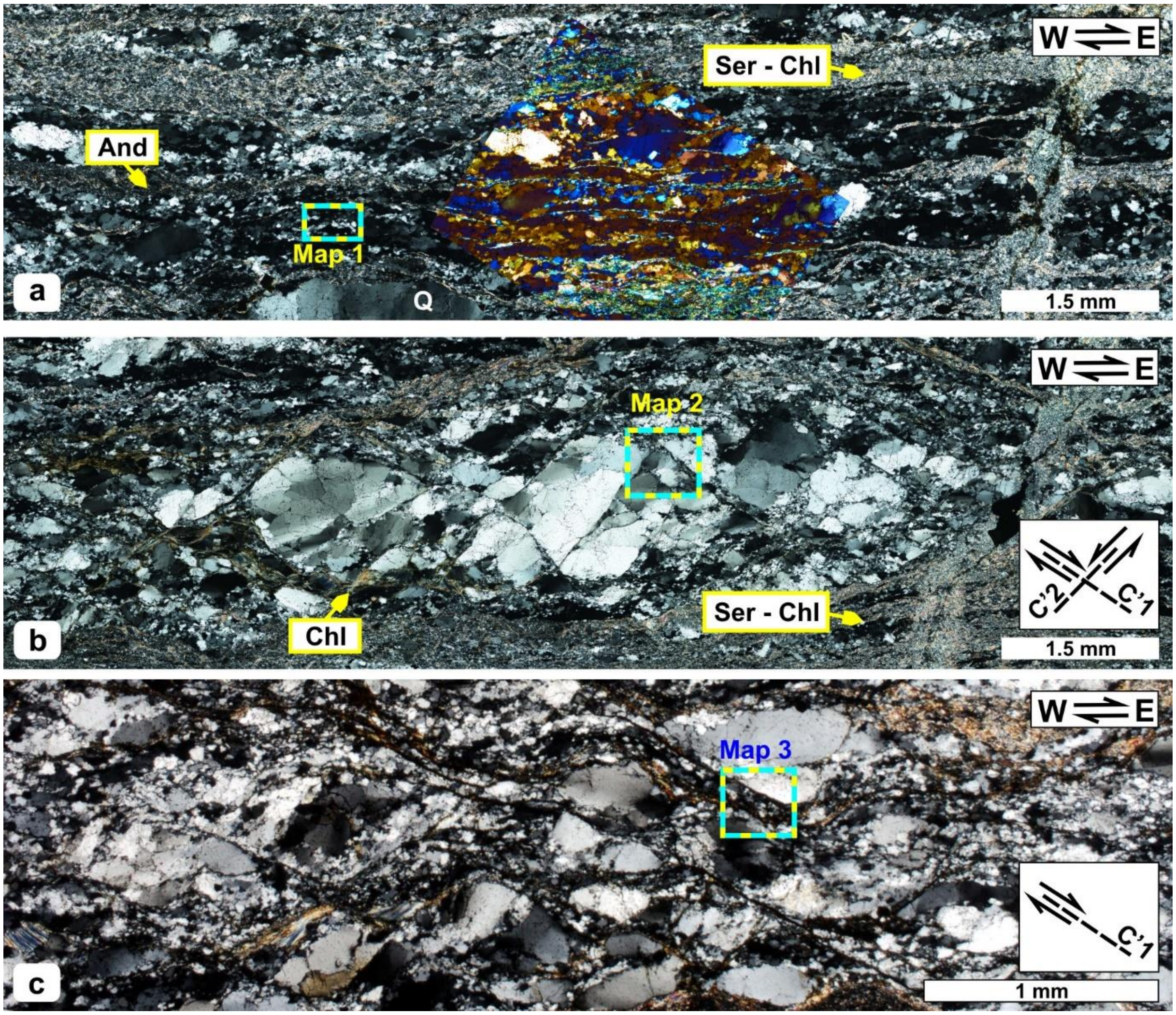

Figure 3 – Microstructures of the investigated sample collected at crossed polarizers. The yellow-cyan boxes highlight the location of EBSD maps. And: andalusite; Chl: chlorite; Q: quartz; Ser: sericite; **(a)** Domain 1: recrystallized subparallel quartz layers interlayered with mica domains and containing large quartz porphyroclasts. The gypsum plate insert highlights the c-axis orientation. **(b)** Domain 2: relic lens of quartz porphyroclasts surrounded by smaller recrystallized grains and cross cut by conjugate shear bands (C'1 and C'2). **(c)** Domain 3: large quartz porphyroclasts surrounded by recrystallized grains, eastwardly dragged along numerous synthetic C' shear bands.

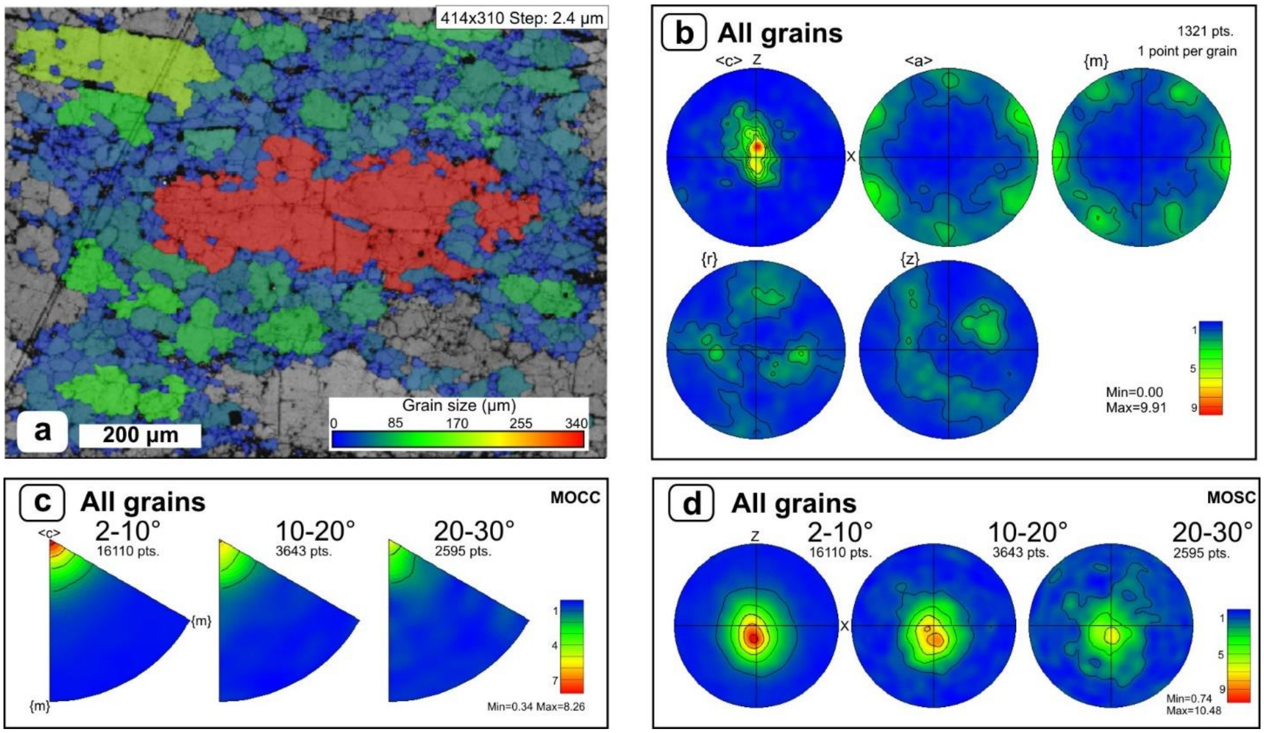

Figure 4 – EBSD analysis of Domain 1. **(a)** Grain size map colored in respect to the legend shown in the lower-right corner. **(b)** Contoured one-point-per-grain pole figures showing the distribution of <c> and <a> axes and poles to {m}, {r} and {z} planes for the complete dataset. **(c-d)** Contoured misorientation axis distribution **(c)** in crystal (MOCC) and **(d)** sample (MOSC) coordinates for 2-10°, 10-20° and 20-30° of misorientation angle for the complete dataset.

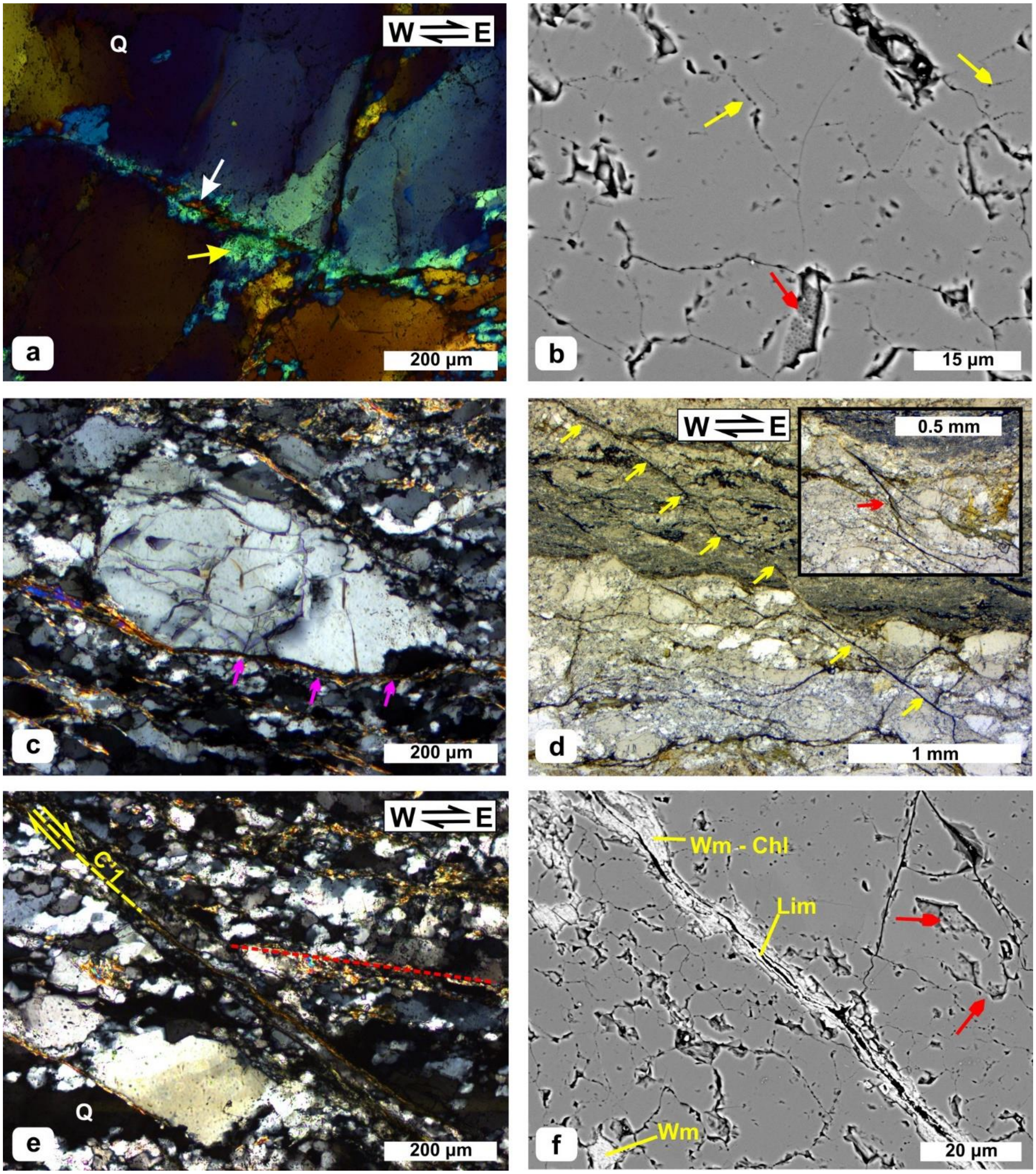

Figure 5 – Microstructures of shear bands. Chl: chlorite; Lim: limonite; Q: quartz; Wm: white mica **(a)** Conjugate shear bands hosted in large quartz porphyroclasts with small grains with similar c-axis orientation (white arrow) and slightly misoriented damaged areas of the host grains (crossed polarizers, gypsum plate). **(b)** SEM BSE-image of grains localized on conjugate shear

bands showing trails of fluid inclusions (yellow arrows) and pitted grain boundaries (red arrow). **(c)** Quartz porphyroclast in Domain 3 mantled by recrystallized grains and phyllosilicate-rich strain caps (purple arrows) showing evident internal microfracturing (crossed polarizers). **(d)** Shear band reactivated as a shear fracture (marked by yellow arrows) with 0.5 mm offset cross cutting the main foliation through several quartz and mica domain. The insert highlights a portion of the same shear fracture where different segments are bridged by en-echelon fractures (parallel polarizers). **(e)** Architecture of a synthetic shear band (C'1; yellow dashed line) characterized by an inner core defined by small quartz grains and a well-defined band of chlorite + white mica (crossed polarizers). The red dashed line traces the foliation. **(f)** SEM BSE-image of a shear band core showing mica inclusions, a straight mica + chlorite + limonite band and pitted grain boundaries (red arrows).

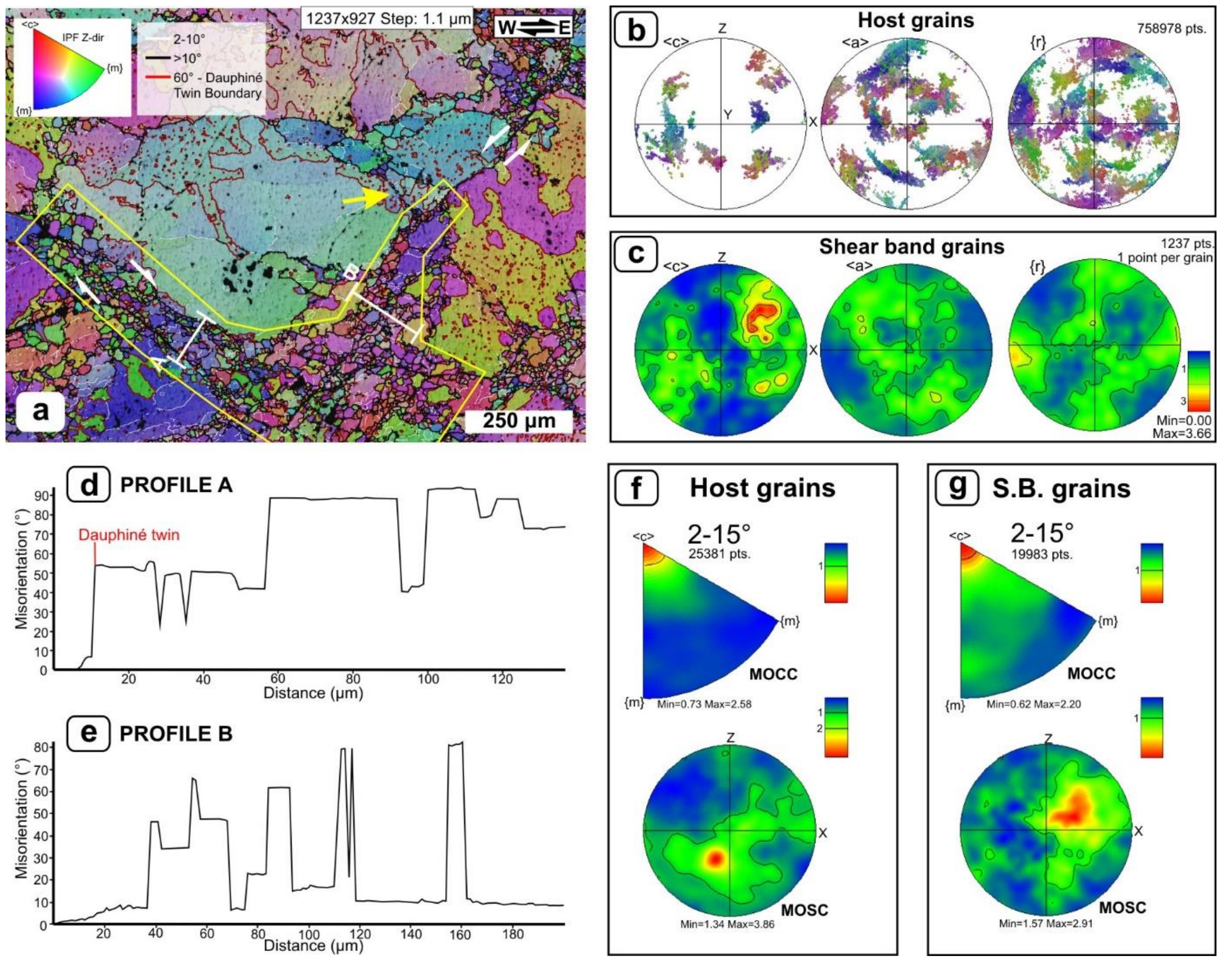

Figure 6 – EBSD analysis of Domain 2. **(a)** Orientation map with color-coding according to the inverse pole figure in the upper-left corner and grain boundaries colored according to the key on top. A and B white lines correspond to misorientation profiles Fig. 6d, e. The yellow arrow flags a small trail of recrystallized grains. White arrows mark the shear sense of conjugate shear bands. The area bound by a yellow line marks the 'shear band grains' subset. **(b-c)** Pole figures showing the orientation of <c> and <a> axes and poles to {r} for **(b)** host grains and **(c)** shear band grains (contoured, one-point-per-grain). **(d-e)** Misorientation profiles for **(d)** profile A and **(e)** profile B (location in Fig. 6a). Relative misorientation with respect to the starting point plotted against distance (µm). **(f-g)** Contoured misorientation axis distribution in crystal (MOCC, above) and

sample (MOSC, below) coordinates for 2-15° of misorientation angle for **(f)** host grains and **(g)** shear band grains subsets.

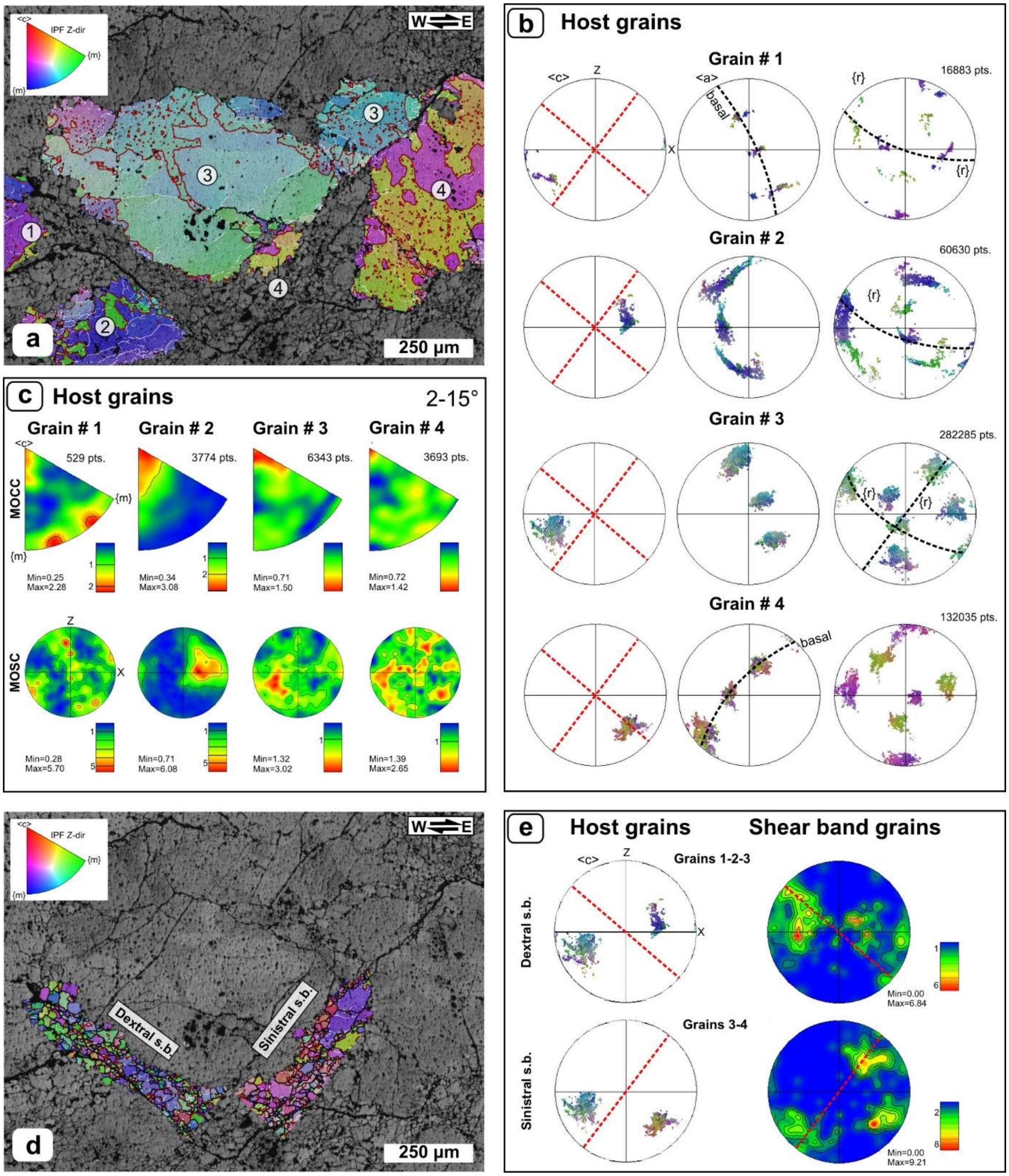

Figure 7 – Relationships between host grains and shear band grains. IPF and grain boundary coloring after Fig. 6a. **(a)** Orientation map indicating four host grains subsets, numbered from 1 to

4. **(b)** Pole figures showing the orientation of <c> and <a> axes and poles to {r} for the host grains subsets. The trace of shear bands is shown with red dashed lines. Crystallographic planes that are subparallel or closely oriented to shear bands are highlighted with black dashed lines. **(c)** Contoured misorientation axis distribution in crystal (MOCC, above) and sample (MOSC, below) coordinates for 2-15° of misorientation angles related to the host grains subsets. **(d)** Orientation map highlighting the dextral and sinistral shear band subsets. **(e)** Comparison between <c> axis pole figures of host grains (left) and contoured one point per grain pole figures for shear band grains (right) relative to the dextral shear band (above) and the sinistral shear band (below). Red dashed lines mark the trace of C' shear bands.

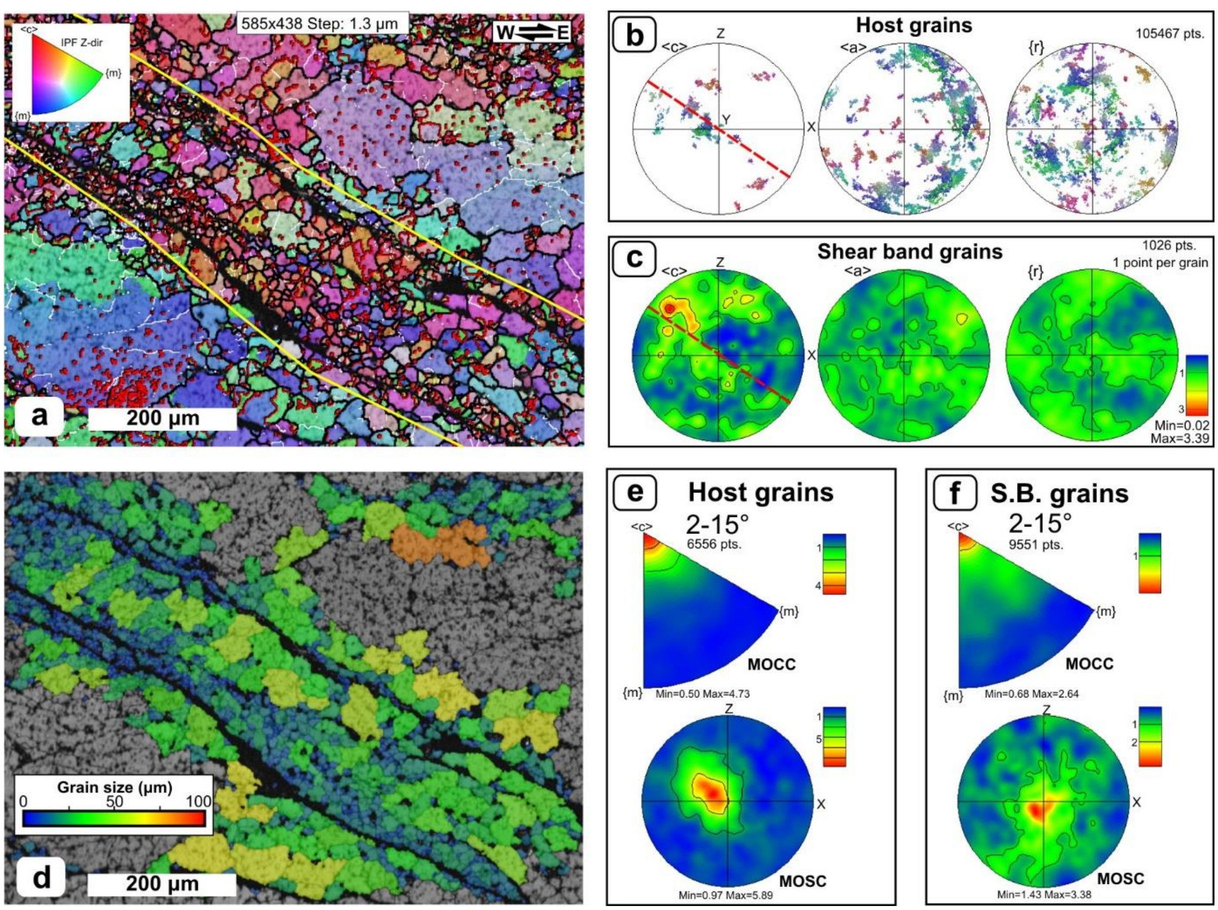

Figure 8 – EBSD analysis of Domain 3. **(a)** Orientation map with IPF and grain boundary coloring as in Fig. 4a. The yellow lines delimitate the shear band grains subset (in the center). **(b-c)** Pole

figures showing the orientation of <c>, <a> axes and poles to {r} for **(b)** host grains and **(c)** shear band grains (contoured, one-point-per-grain). Red dashed lines outline the trace of the shear bands. **(d)** Grain size distribution map showing grains with equivalent circle diameter between 0 and 100 µm, colored as in the lower-left corner key. **(e-f)** Contoured misorientation axis distribution in crystal (MOCC, above) and sample (MOSC, below) coordinates for 2-15° of misorientation angle for **(e)** host grains and **(f)** shear band grains subsets.

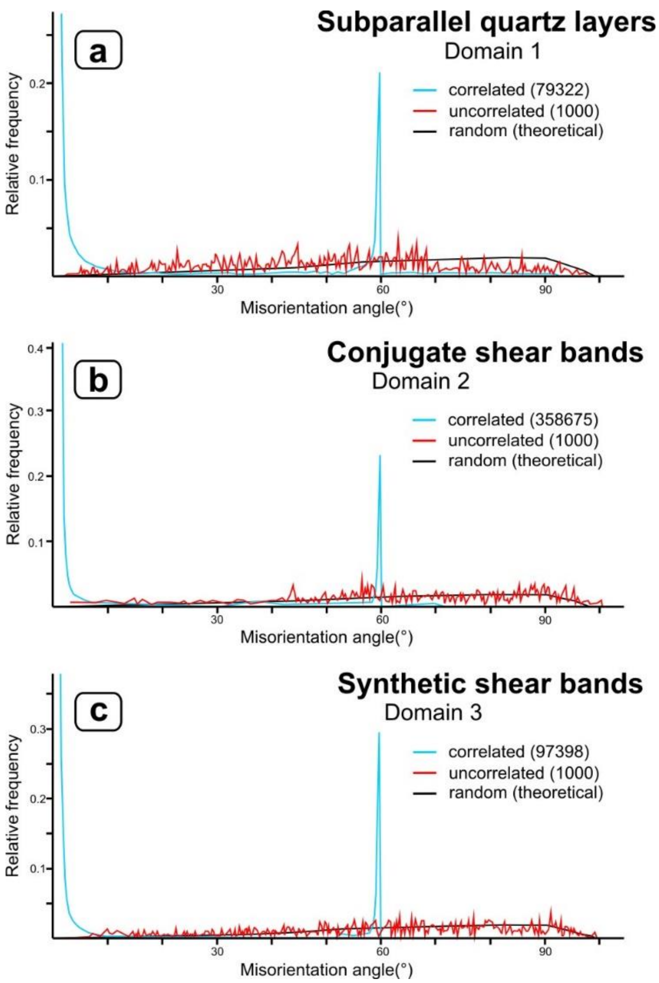

Figure 9 – Misorientation angle distribution (MAD) for correlated (light blue curve), uncorrelated (red curve) and theoretically random (black curve) distributions for EBSD maps: **(a)** Domain 1; **(b)** Domain 2; **(c)** Domain 3.

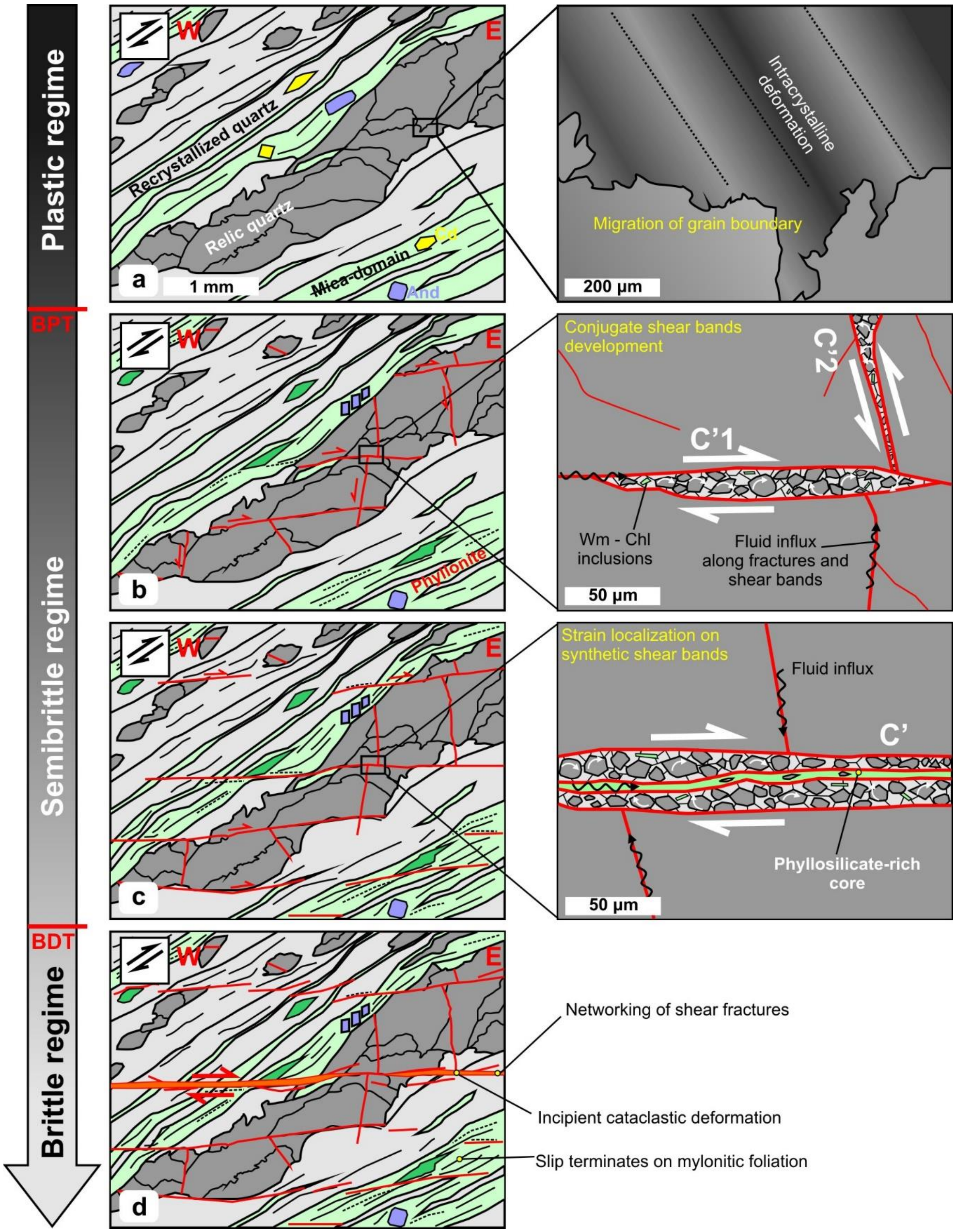

Figure 10 – Sketch diagram showing the reconstructed evolution of the investigated sample in function of time and temperature decrease (dark grey to light grey arrow). BDT: brittle/ductile

transition. BPT: brittle/plastic transition (definitions after Kohlstedt et al., 1995) Steps are: **(a)** Dynamic recrystallization on mylonitic ribbons leaving behind quartz porphyroclasts, **(b)** development of conjugate shear bands in quartz porphyroclasts, **(c)** strain localization on synthetic C' shear bands and **(d)** reactivation of C' shear bands in the brittle regime. See text for a detailed comment.